Numerical Study of Plasma Behavior in a Magnetoplasmadynamic Thruster Around Critical Current

Kenichi Kubota*

Tokyo Institute of Technology, Yokohama, Kanagawa 226-8502, Japan

Ikkoh Funaki†

Japan Aerospace Exploration Agency, Sagamihara, Kanagawa 229-8510, Japan

and

Yoshihiro Okuno‡

Tokyo Institute of Technology, Yokohama, Kanagawa 226-8502, Japan

A self-field magnetoplasmadynamic thruster is numerically studied for an argon mass flow rate of 0.8 g/s. We focus on the plasma behavior around the critical current, at which full propellant ionization is theoretically expected. At a discharge current higher than the critical current, the Hall parameter is large at the anode surface, which leads to an obliquely skewed current profile. This skewed current profile, together with the voltage–current characteristics, show that the Hall effect plays an important role around the critical current. When operating the magnetoplasmadynamic thruster above the critical current, it is shown that the current concentration and the gas density depletion at the anode edge induce a shortage of current carriers. To circumvent the carrier shortage at high discharge currents, we employ a segmented anode. It is found that a segmented anode is effective for suppressing the current concentration and the plasma density depletion on the anode surface without degrading the performance of the thruster.

Nomenclature

B	=	magnetic flux density
b	=	proportionality coefficient of thrust equation
c	=	velocity of light
E	=	electric field
e	=	elementary charge
I	=	unit tensor
J	=	total discharge current
J_c	=	critical current
j	=	current density
k	=	Boltzmann constant
M	=	mass of heavy particles
m_e	=	mass of electron
$\dot{m}$	=	mass flow rate
n_i	=	number density of species i (i-fold ionized species or electron)
p	=	pressure
Q_{ij}	=	collision cross section between particles i, j
q	=	heat flux
R_m	=	magnetic Reynolds number
r	=	radial coordinate
$r_{a,c}$	=	electrode radius (a, anode; c, cathode)
T	=	temperature
U_s	=	internal energy of species s
U_i	=	total ionization energy
u	=	velocity
V	=	voltage
V_i	=	ionization energy from $i-1$ to i-fold ionization level
z	=	axial coordinate
α	=	ionization factor
β_e	=	electron Hall parameter
η	=	generalized coordinate
λ	=	thermal conductivity
μ_0	=	permeability
μ	=	coefficient of viscosity
ν	=	collision frequency
ξ	=	generalized coordinate
ρ	=	mass density
σ	=	electrical conductivity
τ	=	viscous stress tensor
Φ	=	dissipation function

Subscripts

$A1$, $A2$	=	identification of segmented anodes
e	=	electron
em	=	electromagnetic
h	=	heavy particle
J	=	Joule heating
th	=	electron thermal current

*Graduate Student, Department of Energy Sciences.
†Associate Professor, Institute of Space and Astronautical Science. Member AIAA.
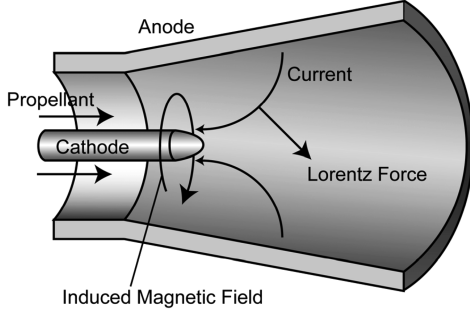‡Professor, Department of Energy Sciences. Member AIAA.

I. Introduction

IN A self-field magnetoplasmadynamic thruster (MPDT), the Lorentz force obtained from the discharge current and the induced magnetic field accelerates the plasma generated by the arc discharge, as shown in Fig. 1. The high thrust density of about 10^4 N/m^2 and the simple configuration of MPDT can reduce the mission trip time and the mass of a spacecraft, hence the self-field MPDT has promising features as a propulsive device for interplanetary exploration. Although many experimental and theoretical efforts regarding the performance improvement have been reported over the past 3 decades, the detailed plasmadynamic phenomena in the thruster and the definite guideline for the electrode design have not yet been specified.

Fig. 1   Principle of a self-field MPD thruster.

Fig. 2   Thruster configuration and computational grid.

The improved availability of sufficient computational power, however, enables us to investigate the detailed plasma flowfields in self-field MPDTs. Princeton University performed a full-scale analysis of a benchmark thruster [1], and Stuttgart University simulated DT2 MPDTs comprising a converging–diverging insulator nozzle and a flared anode at the end of the thruster [2]. Although the preceding research projects adopted argon as a propellant, Mikellides focused on megawatt-class thrusters with hydrogen as a propellant, and computed the flowfield by using the MACH2 code [3].

In Japan, there is abundant experimental data, including the on-orbit demonstration of a pulsed self-field MPDT system in 1995 [4]. In spite of the successful experiment in space, referred to as the Electric Propulsion Experiment (EPEX), detailed investigations on the flowfield of the flared anode type MPDT used in the EPEX experiment have not yet been conducted. Thus, we have developed a numerical code for the purpose of understanding the flowfield of flared anode MPDTs by comparing the numerical results with previously obtained and updated experimental data.

It is recognized that increasing the input power under a fixed mass flow rate can enhance the thrust efficiency of MPDTs [5]. This procedure, however, confronts difficulties above a certain level of the discharge current, the so-called critical current J_c, where the discharge mode transition occurs from a diffused mode to a spot mode, and the voltage waveform begins to fluctuate. Well above the critical current, the operation of MPDTs becomes unstable, accompanied by voltage fluctuations at random frequencies on the order of 1 MHz [6,7]. This suggests that MPDTs should be operated around the critical current defined as follows [8]:

$$J_c^2 = \frac{\dot{m}}{b}\sqrt{\frac{2eV_i}{M}} \qquad b = \frac{\mu_0}{4\pi}\left(\ell_n \frac{r_a}{r_c} + d\right) \qquad (0 < d < \tfrac{3}{4}) \quad (1)$$

However, stable operation far above the critical current is required for the purpose of enhancing the thrust performance. Thus, this paper focuses on the behavior of the plasma and the thrust performance around the critical current. Theoretical [9–12] and experimental [13,14] studies indicate that the instability of the discharge in the thruster above J_c is associated with a shortage of current carriers near the anode surface. In this study, the ratio of the current density to the electron thermal current at the anode edge j/jth, which is employed as an indicator of the carrier shortage, [15] is numerically estimated. Also, because a high j/jth value causes an anode sheath failure, we attempt to suppress the carrier shortage by employing a segmented anode.

II. Physical Modeling

A. Thruster Configuration

The thruster used in this study consists of a short cathode and a flared anode, as shown in Fig. 2. The cathode is 8 mm in diameter and 13 mm in length. The inner diameter of the anode is 28 mm at the inlet and 56 mm at the outlet. The vertical wall located at $z = 45$ mm is composed of an insulating material. This configuration is based on the MPDT whose performance characteristics, such as thrust and
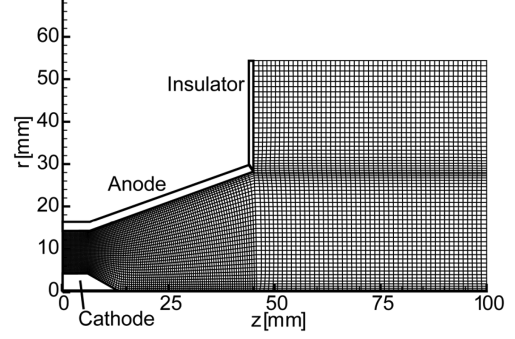
voltage, have been examined by Nakata et al. [16]. Therefore, we can directly compare our results with the experimental results.

We adopt a structured grid with dimensions of 110×35 in the thruster region ($z \leqq 45$ mm) and 50×60 in the plume region ($z \geqq 45$ mm). It is confirmed that the differences in the results for the thrust and the voltage in the case of a finer grid (200×50 in the thruster region and 70×80 in the plume region) are within 1%.

B. Basic Equations

Argon is used as the propellant, and the flow is assumed to be axisymmetric. The governing equations for the plasma flow in a self-field MPDT are introduced on the basis of the following assumptions. We incorporate viscous and thermal diffusive effects, a two-temperature model, and nonequilibrium multivalent ionization processes into our model. The equations are as follows:

Total mass

$$\frac{\partial \rho}{\partial t} + \nabla \cdot (\rho \boldsymbol{u}) = 0 \qquad (2)$$

Mass density of i-fold ion ($i = 1$–6)

$$\frac{\partial \rho_i}{\partial t} + \nabla \cdot (\rho_i \boldsymbol{u}) = \dot{\rho}_i \qquad (3)$$

Momentum

$$\frac{\partial \rho \boldsymbol{u}}{\partial t} + \nabla \cdot \left[\rho \boldsymbol{uu} + \left(p + \frac{B^2}{2\mu_0}\right)\boldsymbol{I} - \frac{\boldsymbol{BB}}{\mu_0}\right] = \nabla \cdot \tau \qquad (4)$$

Heavy particle internal energy

$$\frac{\partial U_h}{\partial t} + \nabla \cdot (U_h \boldsymbol{u}) = -p_h \nabla \cdot \boldsymbol{u} + \Phi - \nabla \cdot \boldsymbol{q}_h + \delta E \qquad (5)$$

Electron internal energy and ionization energy

$$\frac{\partial}{\partial t}(U_e + U_i) + \nabla \cdot [(U_e + U_i)\boldsymbol{u}] = -p_e \nabla \cdot \boldsymbol{u} + \frac{\boldsymbol{j}^2}{\sigma} - \nabla \cdot \boldsymbol{q}_e - \delta E \qquad (6)$$

Induction equation

$$\frac{\partial \boldsymbol{B}}{\partial t} - \nabla \times (\boldsymbol{u} \times \boldsymbol{B}) = -\nabla \times \left[\frac{1}{\mu_0 \sigma} \nabla \times \boldsymbol{B} + \frac{1}{\mu_0 e n_e}(\nabla \times \boldsymbol{B}) \times \boldsymbol{B}\right] \qquad (7)$$

Equation (3) includes a source term corresponding to the ionization rates and the recombination rates [2]. Lotz's formula is used for the forward reaction rates for i-fold ion $k_{f,i}$ [17,18], and the recombination rates $k_{b,i}$ are given from the forward rates and the equilibrium constants $K_i(T_e)$, in which the electron temperature is used because collisions with electrons are the primary processes which determine the ionization fraction:

$$k_{b,i} = \frac{n_i}{n_{i+1}n_e}\bigg|_{\mathrm{eq}} k_{f,i} = \frac{1}{K_i(T_e)}k_{f,i} \qquad (8)$$

$$K_i(T_e) = 2\frac{g^{i+1}}{g^i}\left(\frac{2\pi m_e kT_e}{h^2}\right)^{3/2}\exp\left(-\frac{eV_i}{kT_e}\right) \qquad (9)$$

The source term in Eq. (4) is the viscous term, and the second term in the source term of Eq. (5) is the dissipation function. The internal energy of the heavy particles and the electrons are defined as

$$U_s = \tfrac{3}{2}n_s kT_s \qquad (s = h, e) \qquad (10)$$

The ionization energy is described as follows:

$$U_i = \sum_{j=1}^{6}\sum_{k=1}^{j} V_k n_j \qquad (11)$$

The viscous tensor is given by

$$\tau_{ij} = \mu\left[\left(\frac{\partial u_i}{\partial x_j}+\frac{\partial u_j}{\partial x_i}\right)-\frac{2}{3}\delta_{ij}\frac{\partial u_k}{\partial x_k}\right] \qquad (12)$$

The thermal flux vectors $\boldsymbol{q}_h$, $\boldsymbol{q}_e$ are given by [19]

$$\boldsymbol{q}_h = -\lambda_h \nabla T_h \qquad (13)$$

$$\boldsymbol{q}_e = -\lambda_e \nabla T_e + \frac{5k}{2e}\boldsymbol{j}T_e \qquad (14)$$

The last terms in Eqs. (5) and (6) denote the energy exchange between the heavy particles and the electrons [20]:

$$\delta E = \sum_{s\neq e}\frac{3m_e n_e}{M}\nu_{es}k(T_e - T_h) \qquad (15)$$

The remaining relational expressions necessary for the complete formulation are the generalized Ohm's law, the Ampère's law, and the equation of state:

$$\boldsymbol{j} = \sigma\left(\boldsymbol{E}+\boldsymbol{u}\times\boldsymbol{B}-\frac{1}{en_e}\boldsymbol{j}\times\boldsymbol{B}\right) \qquad (16)$$

$$\nabla\times\boldsymbol{B} = \mu_0\boldsymbol{j} \qquad (17)$$

$$p = p_h + p_e = n_h kT_h + n_e kT_e \qquad (18)$$

The electrical conductivity is given by

$$\sigma = \frac{e^2 n_e}{m_e \nu_{eh}} \qquad (19)$$

where

$$\nu_{eh} = \sum_{s\neq e} n_s Q_{es}\sqrt{8kT_e/\pi m_e} \qquad (20)$$

The cross sections and the viscous and thermal conductivity coefficients are computed using the equations found in [21].

III. Numerical Modeling

A. Numerical Method

The governing Eqs. (2–7) in the preceding section are solved numerically using a time-marching method. All equations are solved following a high-order Lax–Friedrich total variation diminishing (TVD) scheme [22,23]. We select the Lax–Friedrich TVD scheme due to its robustness and the fact that it can be easily applied to any system of conservation equations. To obtain a second-order accuracy with respect to time, predictor–corrector discretization is used in the time integration. The finite volume special discretization is adopted, and the numerical flux on the cell surface is calculated using the MUSCL approach.

B. Discharge Current and Mass Flow Rate

In this study, the discharge current is varied from 4 to 8 kA to examine the behavior of the transition from electrothermal acceleration to electromagnetic acceleration. The propellant injected from the inlet is argon and the prescribed mass flow rate is 0.8 g/s. For the present mass flow rate, the parameter $J^2/\dot{m}$, which is widely known as a key parameter in MPDTs, can be varied from 20 to 80 $(\text{kA})^2/\text{gs}^{-1}$. According to the results from past experiments with argon propellant conducted by Yoshikawa et al. [7], the critical value of the parameter $J^2/\dot{m}$ at which the onset phenomenon occurs is 56 $(\text{kA})^2/\text{gs}^{-1}$ for $\dot{m} = 0.6$ g/s and 36 $(\text{kA})^2/\text{gs}^{-1}$ for $\dot{m} = 3$ g/s.

C. Boundary Conditions

Because the consideration of the plasma ignition at the inlet is difficult to incorporate into the numerical simulation, we ignore the processes and assume a relatively high temperature and high-ionization fraction for the plasma flowing into the thruster. The respective temperatures of the heavy particles and the electrons at the inlet are assumed to be 8000 and 10,000 K, and we set the ionization fraction at the inlet to 0.5. In addition, the pressure is assumed to have a zero gradient in the z direction, and the mass density and the velocity are adjusted so that the mass flow rate is kept constant. The radial distribution of the magnetic flux density at the inlet is obtained from Ampère's law, that is, $B_{in} = -\mu_0 J/2\pi r$, where J is the total discharge current.

Along the wall surfaces, the convective fluxes into the wall are set to zero, and nonslip conditions are applied for the velocity boundary condition. To take into account the heat transfer from the plasma to the wall, we set the temperature of the heavy particles to 1300 K on the anode surface and to 2000 K on the cathode surface. According to the experimental results regarding the radial electron temperature distribution at the outlet under similar operational conditions obtained by Tahara et al. [24], the electron temperature near the wall is estimated to be approximately between 1 and 2 eV. Thus, the temperature T_e of the electrons on the walls is limited to less than 2 eV. For comparison, the cases involving adiabatic conditions for the electron temperature are also calculated to consider the influence of T_e on the wall. In this paper, we denote the former condition as "limited isothermal T_e condition" and the latter as "adiabatic T_e condition." The magnetic flux density on the electrodes is obtained from the condition that the electric field along the wall is zero. By using Ohm's law, this condition reduces to

$$\frac{\partial\psi}{\partial\eta}\left[\frac{\beta_e}{R_m}(\xi_z\eta_z+\xi_r\eta_r)+\frac{1}{R_m}(\xi_z\eta_r-\xi_r\eta_z)\right]$$
$$+\frac{\partial\psi}{\partial\xi}\left[\frac{\beta_e}{R_m}(\xi_z^2+\xi_r^2)\right]=0 \qquad (21)$$

where the velocity on the electrodes is set to zero, and the condition is shown in a dimensionless form. The parameter ψ is rB, and β_e and R_m denote the electron Hall parameter and the magnetic Reynolds number, respectively. The magnetic flux density is set to zero for the insulator. The calculation conditions used in this study are summarized in Table 1.

To examine the sensitivity of the results to the changes in the boundary conditions, we calculate the changes in thrust under

Table 1   Calculation conditions

Propellant	Ar
Mass flow rate, g/s	0.8
Discharge current, kA	4–8
T_h at inlet, K	8000
T_e at inlet, K	10,000
α at inlet	0.5
T_h on anode, K	2000
T_h on cathode, K	1300
T_e on electrodes	Limited isothermal (<2 eV)
	Adiabatic

various conditions at $J = 6$ kA. When the heavy particle temperature at the inlet is set to a lower value of 5000 K, the thrust is reduced by about 1%, and when the ionization fraction at the inlet is set to 0.1, the thrust is reduced by about 3%. When the condition that $T_e < 1$ eV is imposed on the walls, the thrust is reduced by about 2%. Therefore, it is considered that the thrust is insensitive to the particular values set at the boundaries, and this is also true for the other results.

IV. Numerical Results and Discussion

A. Thrust

A comparison of the results for the thrust obtained from our numerical experiment with those from actual experiments is essential for confirming the validity of our code. Figure 3 shows our numerical results and those from the experiments performed by Nakata et al. [16]. The theoretical electromagnetic thrust, which is obtained from Maecher's formula [25]

$$F_{em} = bJ^2 = \frac{\mu_0 J^2}{4\pi}\left(\ln\frac{r_a}{r_c} + d\right) \qquad (0 < d < \tfrac{3}{4}) \qquad (22)$$

is also depicted in the figure, where d depends on the current distribution. Here, r_a and r_c are evaluated at the inlet. If electromagnetic thrust is dominant, the total thrust is considered to approach the theoretical electromagnetic thrust. An approximate numerical evaluation of the thrust is obtained from the momentum flux at the thruster exit:

$$F = \int_{exit}(\rho u^2 + p)\, dS \qquad (23)$$

Here, the contribution of the magnetic pressure is ignored due to its small value at the outlet. We can see that the numerical results for the thrust under the limited isothermal T_e condition are in good agreement with the experimental ones over the entire current range, which indicates that our results are plausible. Figure 3 indicates that the numerical and the experimental results tend to approach the theoretical curve of $d = \tfrac{3}{4}$. Although the thrust in the case of the adiabatic T_e condition might be overestimated, the deviation from the experimental results is about 1 N at most.

Under the condition of the present mass flow rate of 0.8 g/s and the aforementioned thruster configuration, the critical current J_c given by Eq. (1) is about 6 kA, when the parameter d is set to three-quarters. This fact predicts that the acceleration is electrothermal for $J < 6$ kA, and that electromagnetic thrust is dominant for $J > 6$ kA. According to Fig. 3, the numerical results under the limited isothermal T_e condition almost coincide with the theoretical curve above 7 kA, whereas the numerical results differ from the theoretical ones for $J < 6$ kA.

B. Voltage–Current Characteristics

It has been recognized as a common feature that the transition from electrothermal to electromagnetic acceleration entails some changes in the voltage–current characteristics. If a discharge current is lower than the critical current J_c, that is, in the electrothermal acceleration mode, the voltage is linearly proportional to J. At discharge currents higher than J_c, however, the voltage deviates from the linear relation. At the transitional current, the voltage corresponding to the work performed by the Lorentz force is considered to dominate the Joule heating component [5]. When the electromagnetic force is dominant, the voltage should be proportional to the cube of the current as $V \sim b^2 J^3/\dot{m}$. However, the simulation result, which ignores the Hall effect, suggests that the work performed by the Lorentz force is not the main cause for the steep voltage increase [26]. Figure 4 describes the voltage–current characteristics obtained from our numerical results, as well as the experimental results [16]. The results where the Hall effect is not considered are also shown in the figure. The voltage is given by a line integration of the electric field between the anode and the cathode:

$$V = \int_a^c \mathbf{E}\cdot d\mathbf{l} = \int_a^c \left(\frac{\mathbf{j}}{\sigma} - \mathbf{u}\times\mathbf{B} + \frac{1}{en_e}\mathbf{j}\times\mathbf{B}\right)\cdot d\mathbf{l} \qquad (24)$$

Note that this equation does not take into account the sheath voltage, and thus the calculated voltages shown in Fig. 4 must be lower than the experimental results by about 20–30 V [27,28].

As for the experimental results, the voltage increases steeply from 47.4 to 59.6 V as the current increases from 5.2 to 6.6 kA, whereas the increase in voltage corresponding to an increase in current from 4.0 and 5.2 kA is only 1 V. This suggests that the acceleration mode changes from electrothermal to electromagnetic mode around 6 kA.

At currents above J_c, the numerical results calculated by taking into account the Hall effect are significantly higher than those without the Hall effect, which indicates that the Hall effect plays an important role in the steep voltage increase above J_c. This property seems to be consistent with the experimental results. The slope of the V–J curve under the adiabatic T_e condition is similar to that obtained in the experiment. Regarding the numerical results, the fitted curve of the plots for 7, 8 kA indicates that $V \propto J^{2.9}$ under the limited isothermal T_e condition and $V \propto J^{2.8}$ under the adiabatic T_e condition. Interestingly, these results show that our numerical results with the Hall effect support the theoretical presumption ($V \propto J^3$). It should be noted that these results are obtained when the Hall effect was incorporated, although an anode sheath potential drop, which might grow in the range of $J > J_c$, is not taken into account. This steep rise of the voltage is discussed in detail in the next section.

Based on the calculated thrust and voltage, the thrust efficiency can be estimated. We evaluate the thrust efficiency following Eq. (25):
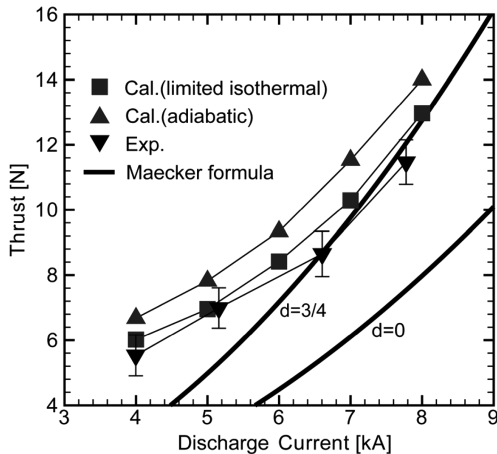

Fig. 3 Thrust as a function of current, Ar, $\dot{m} = 0.8$ g/s. (Limited isothermal and adiabatic denote the limited isothermal T_e condition and adiabatic T_e condition, respectively. Experimental data are from [16].)
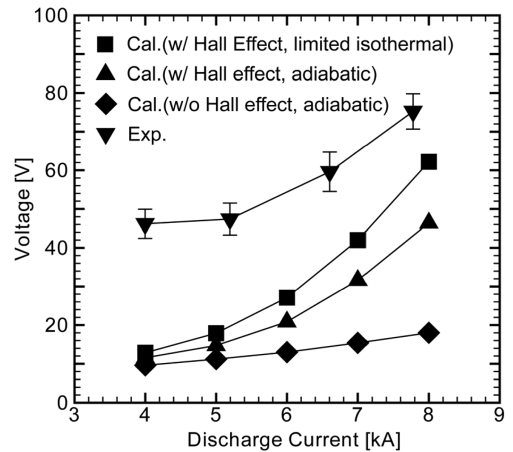

Fig. 4 Voltage–current characteristics, Ar, $\dot{m} = 0.8$ g/s. (Limited isothermal and adiabatic denote the limited isothermal T_e condition and adiabatic T_e condition, respectively. Calculated data do not include the sheath voltage. Experimental data are from [16].)

$$\eta = \frac{F^2 - F^2_{\text{inlet}}}{2\dot{m}J(V + V_s)} \qquad (25)$$

The thrust performance at $J = 6$ kA is described in Table 2. For the evaluation of the thruster efficiency, we assumed a constant sheath voltage $V_s = 20$ V. The thrust efficiency obtained from the experiment is about 13% at $J = 6.5$ kA and 12% at 5.1 kA. Therefore, there is good agreement between the simulation (13.4% at 6 kA) and the experiment.

C. Increase in Discharge Voltage

To clarify the relation between the discharge voltage and acceleration modes, we defined V_J as the voltage corresponding to Joule heating, and V_{em} as a voltage corresponding to the work of the electromagnetic force:

$$JV_J = \int \frac{j^2}{\sigma} \, dV \qquad (26)$$

$$JV_{\text{em}} = \int \boldsymbol{u} \cdot (\boldsymbol{j} \times \boldsymbol{B}) \, dV = JV - JV_J \qquad (27)$$

Here, dV denotes an infinitesimal volume. V_J and V_{em} are presented in Table 3 for the results of the adiabatic T_e condition, where the values in parentheses represent the results without the Hall effect. The ratio of an electromagnetic thrust to the total thrust F_{em}/F is also shown. For $J = 4$ kA, there is no remarkable difference between the results with and without the Hall effect due to the low value of the Hall parameter, as will be shown later. It should be noted that the contribution of V_{em} to V(V_{em}/V) is 20% at most, which leads to a low percentage for the electromagnetic thrust (33%), that is, the thrust is in electrothermal mode. On the other hand, for $J = 7$ kA, each voltage value for which the Hall effect is considered is twice as large as that without the Hall effect. Because the Hall effect causes the extension of the current path, V_J (the Joule heating component) is increased. The current extension due to the Hall effect also serves to increase V_{em}. Comparing the result for $J = 7$ kA with that for $J = 4$ kA, the rate of increase for V_{em} is higher than that for V_J, which results in a relatively high V_{em}/V ratio of 37–40%. This in turn contributes to the high F_{em}/F ratio of 65–69%, that is, the thrust is in electromagnetic mode. However, it should be noted that V_J is larger than V_{em} even for $J = 7$ kA, that is, both V_J and V_{em} contribute to the characteristics of $V \propto J^{2.8}$ (for adiabatic T_e condition). The high F_{em}/F rate, in spite of the fact that $V_J > V_{\text{em}}$, indicates that a large amount of thermal energy is lost as both ionization energy and thermal conduction to the walls.

Table 2 Typical thruster performance (discharge voltage does not include sheath voltage; thrust efficiency is evaluated under the assumption of $V_s = 20$ V)

Discharge current, kA	6
Mass flow rate, g/s	0.8
Thrust, N	8.47
I_{sp}, s	1080
Discharge voltage, V (except for sheath voltage)	27.1
Thrust efficiency, % ($V_s = 20$)	13.4

Table 3 Summary of voltages and ratio of electromagnetic force to total thrust; values in parentheses represent results without the Hall effect (limited isothermal T_e condition is adopted)

Current	V, V	V_J, V	V_{em}, V	V_{em}/V, %	F_{em}/F, %
4 kA	11.6	9.8	1.8	15.7	33.4
	(9.6)	(7.7)	(1.9)	(19.5)	(33.6)
7 kA	31.7	20.0	11.7	36.9	65.2
	(15.4)	(9.2)	(6.2)	(40.3)	(69.1)

a)

b)
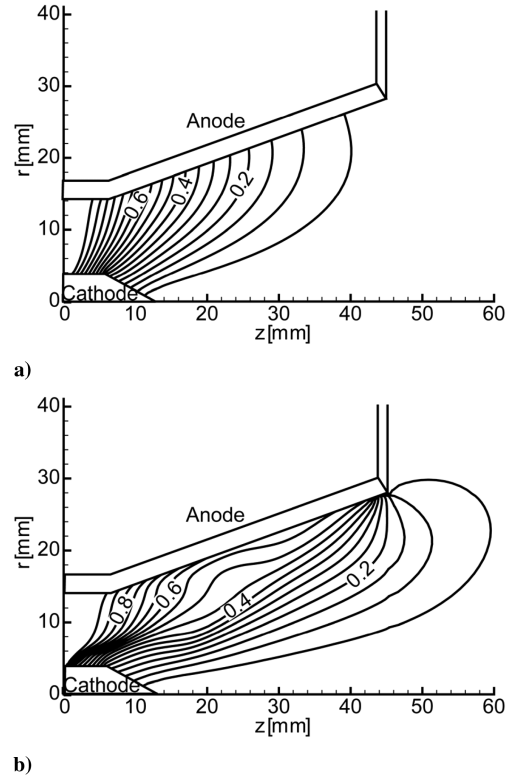
Fig. 5 Current contour lines, Ar, $\dot{m} = 0.8$ g/s: a) $J = 4$ kA, b) $J = 7$ kA. (Labeled values on the contour lines denote the ratio of the current flowing downstream region to the total discharge current. Limited isothermal T_e condition is adopted.)

D. Flowfield

In this section, the flowfields around the critical current are discussed. All figures shown here (Figs. 5–8) present results obtained under the limited isothermal T_e condition.

To examine the change in the flowfield around the critical current, we compare the flowfields for $J = 4$ and 7 kA. Figure 5 shows the current path, which is equivalent with the contour lines of the function $|rB|$. The labeled values on the contour lines denote the ratio of the current flowing downstream viewed from the line to the total discharge current. For $J = 4$ kA, the numerical results indicate that the current does not spread out of the thruster, and no current spot is found on the electrodes, that is, the current distribution on the electrodes is diffused. On the other hand, when $J = 7$ kA, which is above the critical current, the current path is drastically different from that in the case of $J = 4$ kA, where the current lines concentrate at the anode edge ($z = 45$ mm, $r = 28$ mm) and the cathode root ($z = 0$–6 mm, $r = 4$ mm). Although the current lines whose labels are less than 0.6 tend to concentrate near the anode edge for $J = 7$ kA, the current lines above 0.6 are similar in the two cases ($J = 4$ kA and 7 kA). Around the middle part of the flared anode surface ($z \approx 25$ mm), the electrons are prevented from flowing into the anode and are carried downstream. The obliquely skewed current lines are attributed to the Hall effect.

In Fig. 6, the respective Hall parameter distributions at $J = 4$ and 7 kA are described. When $J = 4$ kA, the Hall parameter is less than unity in the discharge chamber, and it is highest at the cathode root because the induced magnetic flux density is largest there. Because the Hall parameter is relatively low inside the thruster, a noticeable distortion of the current lines due to the Hall effect does not appear for $J = 4$ kA. On the other hand, in the case of $J = 7$ kA, the current distribution changes into a different one, as shown in Fig. 5b. At the cathode root, the Hall parameter is about six. However, it decreases steeply down to 1–2 around the downstream region near the cathode surface, due to the appearance of a high-density region, as will be shown later. Moreover, it should be noted that the region where the Hall parameter is high appears around the anode surface of the nozzle
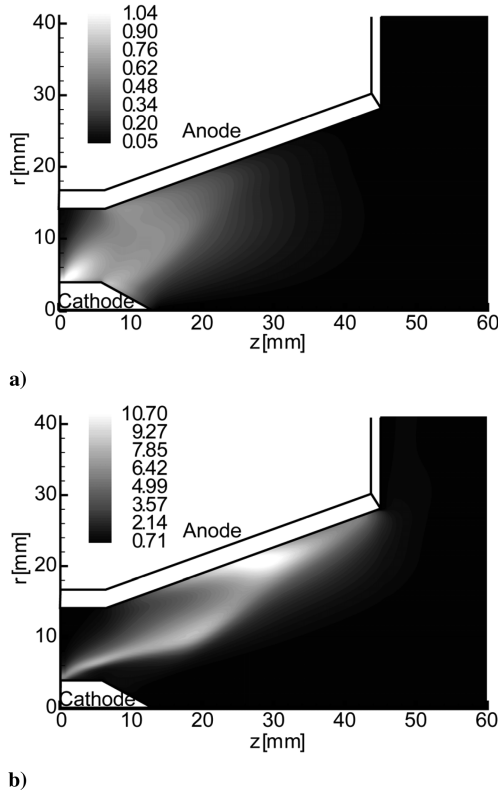
Fig. 6   Hall parameter, Ar, $\dot{m} = 0.8$ g/s: a) $J = 4$ kA , b) $J = 7$ kA. (Limited isothermal T_e condition is adopted.)
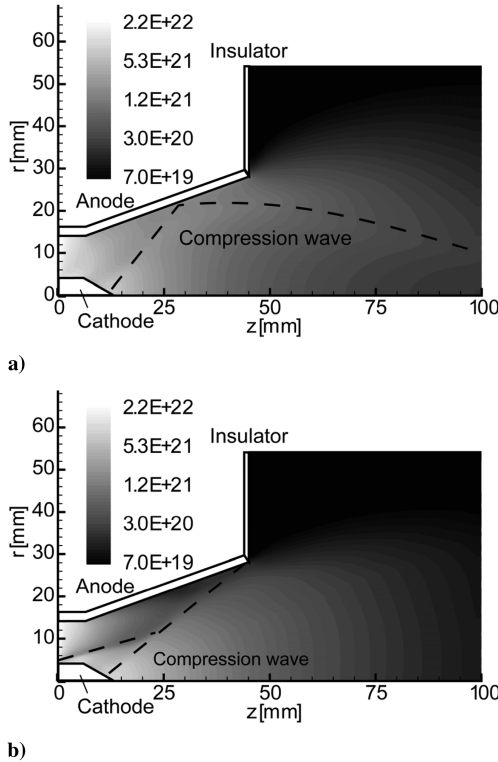

Fig. 7   Number density of heavy particles (neutral and ions), m^{-3}, Ar, $\dot{m} = 0.8$ g/s: a) $J = 4$ kA, b) $J = 7$ kA. (Limited isothermal T_e condition is adopted.)

(diverging part). The highest value of the Hall parameter amounts to 11.4 around $z = 28$ mm, $r = 20$ mm, whereas the Hall parameter at the same location in the case of $J = 4$ kA is about 0.1. Because the electrons in the region where the Hall parameter is high are forced to

flow downstream by the Hall effect, they are prevented from flowing into the anode. As a result, the current lines around the region tend to be parallel to the anode surface, which leads to the intensive concentration of current at the anode edge. A steep increase in the Hall parameter in the vicinity of the anode surface for an increasing current around the critical current was also observed in an MPDT experiment conducted by Diamant et al. at Princeton [29].

The high Hall parameter around $z = 28$ mm, $r = 20$ mm is attributed to the low number density in that region. Figure 7 describes the number density of heavy particles in both cases ($J = 4$ and 7 kA). At $J = 4$ kA, the number density at $z = 28$ mm, $r = 20$ mm is about 1.7×10^{21} m^{-3}. When $J = 7$ kA, however, the number density of heavy particles is about 1.6×10^{20} m^{-3}. Because the Hall effect leads to the current profile being parallel to the anode surface, the Lorentz force perpendicular to the anode surface provokes the density depletion.

We can also see from Fig. 7 that a compression wave extends from the cathode tip. At $J = 4$ kA, the weak compression wave propagates toward the anode surface and is reflected around $z = 30$ mm. After that, the reflected compression wave propagates toward the axis of symmetry, which leads to the density distribution in the plume region, shown in Fig. 7a. On the other hand, the structure of the density distribution in the case of $J = 7$ kA differs from that in the case of $J = 4$ kA. There is a compression wave for $J = 7$ kA starting from the cathode root. It is notable that the direction of the compression wave is slightly varied around $z = 20$ mm, $r = 9$ mm due to another compression wave extending from the vicinity of the cathode tip. Although the combined compression wave reaches the anode surface, there is no reflected compression wave in the plume region.

Figure 8 shows the velocity distribution and the streamlines for $J = 7$ kA. The plasma is accelerated toward the axis of symmetry, after which it is compressed, leading to a high-velocity cathode jet as a result of the so-called pumping force. The current profile near the cathode root shown in Fig. 5b causes the strong compression of the plasma onto the cathode surface because the magnitude of the Lorentz force is the highest near the cathode root.

E.   Carrier Shortage on Anode Surface

In the previous section, we have shown that the plasma density near the anode surface is drastically decreased for currents higher than J_c. This plasma depletion on the anode surface is considered to result in a shortage of current carriers. The theory addressing the issue of carrier shortage, the so-called anode starvation theory, uses the ratio of the net current density perpendicular to the anode surface (which we denote as j) to the electron thermal current $j_{th} = en_e C_e / 4$ as an indicator of the carrier shortage, where C_e denotes the electron thermal speed $\sqrt{8kT_e/m_e\pi}$. If j is less than j_{th}, an ion-rich sheath forms so that the flow of electrons to the anode is prevented (Fig. 9). On the other hand, if j exceeds j_{th}, an electron-rich sheath forms that drives the electrons to the anode due to the lack of electrons as current carriers, which leads to a large energy input on the anode surface and significant evaporation of the anode material. Regarding the experimental evidence of the preceding prediction, Hügel [13] and
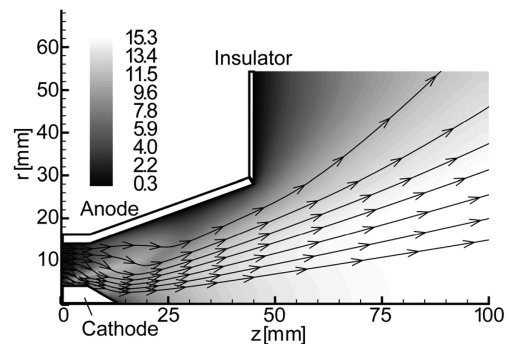

Fig. 8   Velocity contours and streamlines, km/s, Ar, $\dot{m} = 0.8$ g/s, $J = 7$ kA. (Limited isothermal T_e condition is adopted.)
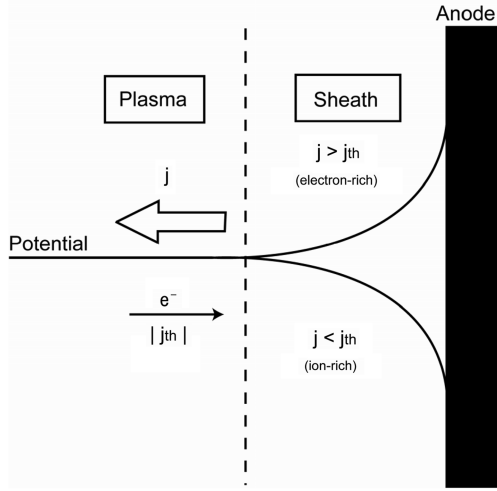
Fig. 9   Relationship among current, electron thermal current, and potential near anode surface.

Kurtz [14] specified that the voltage drop at the anode changes its sign around the critical current. In addition, Diamant et al. [29] and Gallimore et al. [30] showed that anode starvation is closely related to the Hall parameter. To discuss this phenomenon, we describe the current density perpendicular to the anode and the ratio of the current density to the electron thermal current at the anode edge ($z = 45$ mm, $r = 28$ mm) as a function of discharge current in Fig. 10. Because the respective current densities for $J = 4$ and 5 kA are low, the ratio j/j_{th} is also kept low. At $J = 6$ kA, which approximately corresponds to the critical current, j/j_{th} begins to increase, and at $J = 7$ kA, the ratio j/j_{th} under the limited isothermal T_e condition rises steeply to about unity, due to both the concentration of the current and the depletion of the gas density on the anode surface. When the discharge current is increased further, the j/j_{th} value keeps rising, taking a value of about 1.9 at $J = 8$ kA. It is noted that this tendency can be seen even under the adiabatic T_e condition, although the rate of increase is lower. This abrupt rise of the j/j_{th} value does not appear unless the Hall effect is taken into account.

There are analytical expressions for J_c in terms of the anode starvation theory [9–11]. Baksht et al. investigated the anode starvation analytically under the assumption that the radial current is equal to electron thermal current, and derived the relational expression for the critical current as follows [9]:

$$J_c^7 = 1.17c^8 e \frac{kT\dot{m}^4R^3}{\sigma M^2 d^4}\frac{L}{d} \tag{28}$$
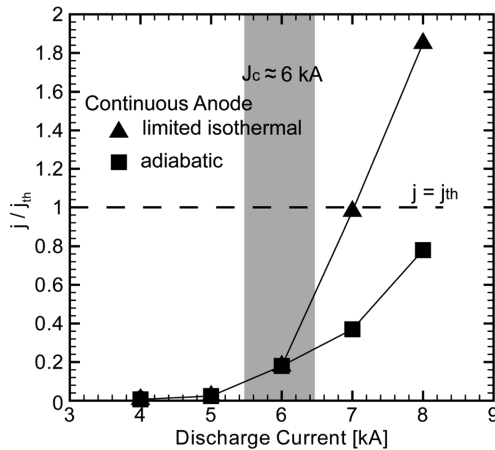

Fig. 10   Ratio of current density to electron thermal current at the anode edge, Ar, $\dot{m} = 0.8$ g/s. (Limited isothermal and adiabatic denote the limited isothermal T_e condition and adiabatic T_e condition, respectively.)

where the unit is the centimeter-gram-second system. R, d, and L are the mean channel radius, the electrode gap, and the channel length, respectively, where $R \gg d$ is assumed. We discuss the critical current given by Baksht et al.'s expression in Eq. (28), although $R \gg d$ is not satisfied in our case. If we set the parameters to $d = 17$ mm (average value), $L = 45$ mm, $R = 9$ mm, $T = 2$ eV, and $\sigma = 5000$ S/m, Baksht et al.'s critical current is estimated as 5.9 kA. Although this value depends on the input parameter, J_c varies between 5 and 7 kA. It is notable that the critical current presumed from our results is almost the same as the value for J_c obtained by Baksht et al.'s model.

F.   Segmented Anode

Although the anode density depletion can be circumvented by reducing the nozzle angle or by changing the electrode size, such measures also affect the thrust characteristics (the thrust is expected to decrease). To avoid the carrier shortage without changing the geometry of the thruster, we employ a segmented anode as shown in Fig. 11. Let us denote each anode as $A1$ and $A2$, respectively, and assume that an external electrical circuit can divide the discharge current equally between the two anodes, that is, $J_{A1}:J_{A2} = 1:1$. We can adjust the magnitude of the current at each electrode by using two half-scale power sources for each anode, or by employing ballast resistances with one power source. The anode is segmented by placing an insulator at $z = 20$–30 mm. With this geometry, we can expect not only the elimination of the current concentration around the thruster exit, but also the suppression of the plasma density depletion on the nozzle surface without reducing the nozzle angle. The segmented anode technique was employed by Kurtz et al. for the straight anode configuration, although the current at each electrode was not prescribed [14]. The magnetic flux density along the insulated part between $A1$ and $A2$ is given by Ampère's law, that is, $B = -\mu_0 J_{A2}/2\pi r$. The limited isothermal condition is adopted as the boundary condition for the electron temperature.

Although the values of the thrust and the thrust efficiency for the continuous anode and the segmented anode were almost the same ($F = 8.4$ N, $\eta = 12.9\%$), the flowfield structures are different in each case. Figure 12 shows the current path for $J = 7$ kA. Because
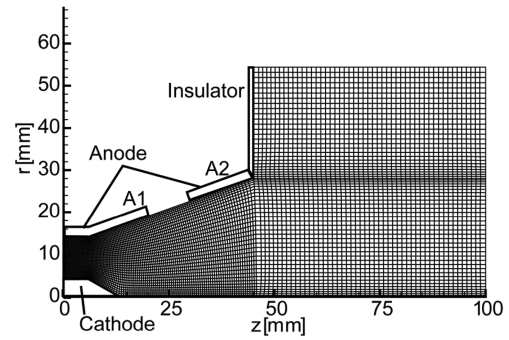

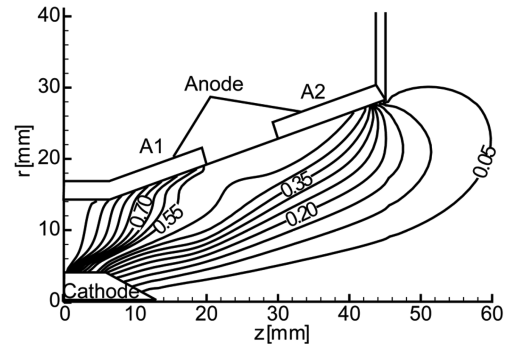
Fig. 11   Segmented anode configuration.

Fig. 12   Current contour lines with segmented anodes, Ar, $\dot{m} = 0.8$ g/s, $J = 7$ kA. (Ratio of each discharge current for $A1$, and $A2$ is 1:1.)
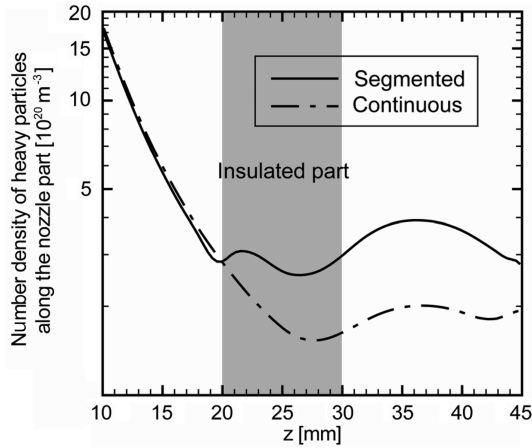
Fig. 13 Comparison of number density of heavy particles along the nozzle part with segmented and continuous anode, Ar, $\dot{m} = 0.8$ g/s, $J = 7$ kA.
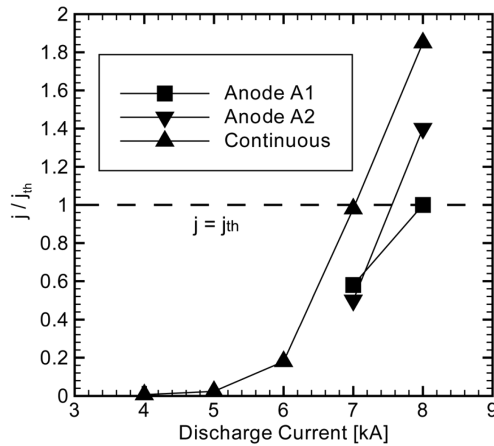

Fig. 14 Ratio of current density to electron thermal current at the anode edge for segmented and continuous anode, Ar, $\dot{m} = 0.8$ g/s (limited isothermal T_e condition).

the discharge current of $A1$ does not expand significantly toward the downstream region, the current density at the edge of $A2$ is moderated to 4.2×10^6 A/m^2, whereas it is 6.0×10^6 A/m^2 in the case of the continuous anode. In comparison to the continuous anode case, the current along the insulator surface, and hence the radial Lorentz force, is reduced in the case of the segmented anode. Thus, plasma depletion around the anode nozzle surface is not observed. Figure 13 shows the number density of heavy particles along the anode nozzle surface from $z = 10$ to 45 mm. In the case of the continuous anode, the density decreases monotonically due to the nozzle expansion in the region of $z < 28$ mm. Because the flow near the anode surface is subsonic, the density is recovered at $z \approx 28$ mm due to the backward propagation of the disturbance induced by the compression wave extending from the cathode tip. A decrease in the density is not observed at the end of $A1$ for the segmented anode.

Figure 14 shows the respective values of j/j_{th} at the edge of $A1$ and $A2$ for $J = 7$ and 8 kA. At $J = 7$ kA, the j/j_{th} value at the edge of $A2$ decreases from 1 to 0.5 in the case of the segmented anode. This is due to a low current density, and hence the weak Lorentz force, which leads to a higher gas density in comparison to the continuous anode. Even at the edge of $A1$, the j/j_{th} value is below 0.6. Therefore, it is considered that a segmented anode can be useful for preventing high current concentration at the anode edge.

V.   Conclusions

We performed a numerical examination of the plasma behavior in a magnetoplasmadynamic thruster over a wide operation range

around the critical current for an argon mass flow rate of 0.8 g/s. To compare the respective plasma flows in electrothermal and electromagnetic acceleration modes, we compared two results, $J = 4$ and 7 kA, where the critical current is about 6 kA. Along the anode surface, the Hall parameter increases together with the current, leading to an obliquely skewed current profile at discharge currents higher than the critical current. In this case, an increase in the radial component of the Lorentz force induces the depletion of the gas density around the anode surface, which corresponds to a shortage of current carriers. A steep increase in the ratio of the current density to the electron thermal current at the anode edge around the critical current indicates the occurrence of a carrier shortage. It is also shown that the Hall effect is predominantly attributed to the steep increase in the voltage around the critical current.

To avoid the density depletion at the anode surface, a segmented anode is employed in the numerical simulation. The segmented anode leads to the suppression of the current concentration and entails the enhancement of the number density at the anode. A segmented anode is therefore considered suitable for realizing a stable discharge for currents above the critical current.

References

[1] Sankaran, K., Choueiri, E. Y., and Jardin, S. C., "Comparison of Simulated Magnetoplasmadynamic Thruster Flowfields to Experimental Measurements," *Journal of Propulsion and Power*, Vol. 21, No. 1, 2005, pp. 129–138.
doi:10.2514/1.5340
[2] Heiermann, J., and Auweter-Kurtz, M., "Numerical and Experimental Investigation of the Current Distribution in Self-Field Magnetoplasmadynamic Thrusters," *Journal of Propulsion and Power*, Vol. 21, No. 1, 2005, pp. 119–128.
doi:10.2514/1.5227
[3] Mikellides, P. G., "Modeling and Analysis of a Megawatt-Class Magnetoplasmadynamic Thruster," *Journal of Propulsion and Power*, Vol. 20, No. 2, 2004, pp. 204–210.
doi:10.2514/1.9246
[4] Toki, K., Shimizu, Y., and Kuriki, K., "On-Orbit Demonstration of a Pulsed Self-Field Magnetoplasmadynamic Thruster System," *Journal of Propulsion and Power*, Vol. 16, No. 5, 2000, pp. 880–886.
doi:10.2514/2.5655
[5] Lapointe, M. R., Strzempkowski, E., and Pencil, E., "High Power MPD Thruster Performance Measurements," AIAA Paper 2004-3467, 2004.
[6] Kuriki, K., and Suzuki, H., "Transitional Behavior of MPD Arcjet Operation," *AIAA Journal*, Vol. 16, No. 10, 1978, pp. 1062–1067.
doi:10.2514/3.61004
[7] Yoshikawa, T., Kagaya, Y., and Kuriki, K., "Thrust and Efficiency of the K-III MPD Thruster," *Journal of Spacecraft and Rockets*, Vol. 21, No. 5, 1984, pp. 481–487.
doi:10.2514/3.25683
[8] Choueiri, E., "Scaling of Thrust in Self-Field Magnetoplasmadynamic Thrusters," *Journal of Propulsion and Power*, Vol. 14, No. 5, 1998, pp. 744–753.
doi:10.2514/2.5337
[9] Baksht, F. G., Moizhes, B. Ya., and Rybakov, A. B., "Critical Regime of a Plasma Accelerator," *Soviet Physics–Technical Physics*, Vol. 18, No. 12, 1974, pp. 1613–1616.
[10] Korsun, A. G., "Current Limiting by Self-Magnetic Field in a Plasma Accelerator," *Soviet Physics–Technical Physics*, Vol. 19, No. 1, 1974, pp. 124–126.
[11] Shubin, A. P., "Dynamic Nature of Critical Regimes in Steady-State High-Current Plasma Accelerators," *Soviet Journal of Plasma Physics*, Vol. 2, No. 1, 1976, pp. 18–21.
[12] Niewood, E. H., and Martinez-Sanchez, M., "The Hall Effect in a Numerical Model of MPD Thrusters," *22nd International Electric Propulsion Conference*, Paper 91-099, Oct. 1991.

[13] Hügel, H., "Effect of Self-Magnetic Forces on the Anode Mechanism of a High Current Discharge," *IEEE Transactions on Plasma Science*, Vol. 8, No. 4, 1980, pp. 437–442.
doi:10.1109/TPS.1980.4317353

[14] Kurtz, H. L., Auweter-Kurtz, M., Merke, W. D., and Schrade, H. O., "Experimental MPD Thruster Investigation," AIAA Paper 87-1091, 1987.

[15] Lawless, J. L., and Subramaniam, V. V., "A Review of the Theory of Self-Field MPD Thrusters," *22nd International Electric Propulsion Conference*, Paper 91-019, Oct. 1991.

[16] Nakata, D., Toki, K., Funaki, I., Shimizu, Y., Kuninaka, H., and Arakawa, Y., "Experimental Verification for the Nozzle Shape Optimization of the Self-Field MPD Thruster," *29th International Electric Propulsion Conference*, Electric Rocket Propulsion Society Paper IEPC-05-163, Oct. 2005.

[17] Lotz, W., "Electron-Impact Ionization Cross-Sections and Ionization Rate Coefficients for Atoms and Ions from Hydrogen to Calcium," *Zeitschrift für Physik*, Vol. 216, No. 3, 1968, pp. 241–247.
doi:10.1007/BF01392963

[18] Lotz, W., "Subshell Binding Energies of Atoms and Ions from Hydrogen to Zinc," *Journal of the Optical Society of America*, Vol. 58, No. 7, 1968, pp. 915–921.
doi:10.1364/JOSA.58.000915

[19] Sutton, G. W., and Sherman, A., *Engineering Magnetohydrodynamics*, Dover, New York, 2006.

[20] Mitchner, M., and Kruger, C. H., *Partially Ionized Gases*, Wiley-Interscience, New York, 1973.

[21] Boie, C., Auweter-Kurtz, M., Kaeppeler, H. J., and Sleziona, P. C., "Numerical Investigation of MPD Thrusters with Unstructured Mesh Methods," *24th International Electric Propulsion Conference*, Electric Rocket Propulsion Society Paper IEPC-95-168, Sept. 1995.

[22] Tóth, G., and Odstrčil, D., "Comparison of Some Flux Corrected Transport and Total Variation Diminishing Numerical Schemes for Hydrodynamic and Magnetohydrodynamic Problems," *Journal of Computational Physics*, Vol. 128, No. 1, 1996, pp. 82–100.
doi:10.1006/jcph.1996.0197

[23] Yee. H. C., "A Class of High-Resolution Explicit and Implicit Shock-Capturing Methods," NASA TM-101088, 1989.

[24] Tahara, H., Kagaya, Y., and Yoshikawa, T., "Exhaust Plume Characteristics of Quasi-Steady MPD Thrusters," *27th International Electric Propulsion Conference*, Electric Rocket Propulsion Society Paper IEPC-01-133, Oct. 2001.

[25] Jahn, R. G., *Physics of Electric Propulsion*, Dover, New York, 2006.

[26] Kubota, K., Funaki, I., and Okuno, Y., "Numerical Investigation of Ionization and Acceleration Processed in a Self-Field MPD Thruster," *29th International Electric Propulsion Conference*, Electric Rocket Propulsion Society Paper IEPC-05-089, Oct. 2005.

[27] Kuriki, K., Onishi, M., and Morimoto, S., "Thrust Measurement of K-III MPD Arcjet," *AIAA Journal*, Vol. 20, No. 10, 1982, pp. 1414–1419.
doi:10.2514/3.51201

[28] Nakata, D., Toki, K., Shimizu, Y., Funaki, I., Kuninaka, H., and Arakawa, Y., "An Experimental Study of the Electrode Fall Voltage in an MPD Thruster," *30th International Electric Propulsion Conference*, Electric Rocket Propulsion Society Paper IEPC-07-115, Sept. 2007.

[29] Diamant, K. D., Choueiri, E. Y., and Jahn, R. G., "Spot Mode Transition and the Anode Fall of Pulsed Magnetoplasmadynamic Thrusters," *Journal of Propulsion and Power*, Vol. 14, No. 6, 1998, pp. 1036–1042.
doi:10.2514/2.5371

[30] Gallimore, A. D., Kelly, A. J., and Jahn, R. G., "Anode Power Deposition in Magnetoplasmadynamic Thrusters," *Journal of Propulsion and Power*, Vol. 9, No. 3, 1993, pp. 361–368.
doi:10.2514/3.23630

E. Choueiri
Associate Editor